ARTICLE

Open Access

Growth of two-dimensional Janus MoSSe by a single in situ process without initial or follow-up treatments

Chan Wook Jang[1], Won Jun Lee[1], Jae Kuk Kim[1], Sang Minh Park[1], Sung Kim[2] and Suk-Ho Choi[1]

Abstract

Two-dimensional (2D) Janus transition metal dichalcogenides (TMDCs) are highly attractive as an emerging class of 2D materials, but only a few methods are available for fabricating them. These methods rely on the initial growth of 2D TMDCs in one process, followed by an additional plasma or high-temperature (T) process. To overcome these drawbacks, we employ the new approach of NaCl-assisted single-process chemical vapor deposition, which consists of three steps that proceed only by altering the temperature in situ. In the first step, MoS_2 is deposited onto a SiO_2/Si substrate with the Mo and S atoms activated in different temperature zones. In the second step, S vacancies are formed in the upper layer of the grown MoS_2 by annealing. In the third step, the vacancies are filled with activated Se atoms. Throughout the steps, NaCl lowers the melting point of the constituent atoms, while the T in each zone is properly controlled. The growth mechanism is clarified by a separate annealing experiment that does not involve a supply of activated atoms. These results highlight a simple and cost-effective approach for growing Janus MoSSe, which is more useful for fundamental studies and device applications.

Introduction

Two-dimensional (2D) Janus transition metal dichalcogenides (TMDCs) have recently attracted increasing attention as an emerging class of 2D materials. The transition metal layer of Janus 2D TMDCs is sandwiched by two different chalcogen layers, resulting in broken mirror symmetry along the out-of-plane direction, which distinguishes Janus 2D TMDCs from pristine TMDCs. This unique characteristic of 2D Janus TMDCs leads to their novel phenomena, such as Rashba spin splitting, piezoelectric polarization, second-harmonic generation, catalytic effects, and long carrier recombination[1-7], which are very promising for their application in sensors, actuators, piezo/thermal-electric devices, solar cells, ion batteries, and other electromechanical devices[8-11]. The asymmetry of Janus TMDCs has also been used to tailor the van der Waals (vdW) interlayer coupling and charge transfer in vdW heterostructures[12-15]; such tailoring of Janus $MoSSe/MoS_2$ heterobilayers was performed by tuning the twist angle and interface composition[16]. The energy of graphene plasmons in vdW Janus MoSSe/graphene heterostructures was engineered up to 0.5 eV by varying the number of Janus MoSSe layers[17].

The synthesis technology of 2D Janus TMDCs has not yet been established, but recently, monolayer (ML) Janus MoSSe was successfully grown by controllably substituting S or Se atoms on the surface of a MoS_2 or $MoSe_2$ layer with Se or S atoms, respectively, based on two major approaches[18,19]. It is common for both materials, MoS_2 and $MoSe_2$, to be grown as a ML in a separate process. In one approach, the top S layer in the pregrown MoS_2 2D sheet was stripped and replaced with H atoms, and the H atoms were then thermally selenized under vacuum[18]. In

Correspondence: Suk-Ho Choi (sukho@khu.ac.kr)
[1]Department of Applied Physics, Institute of Natural Sciences, and Integrated Education Institute for Frontier Science and Technology (BK21 Four), Kyung Hee University, Yongin 17104, Korea
[2]Humanitas College, Department of Physics, and Integrated Education Institute for Frontier Science and Technology (BK21 Four), Kyung Hee, University, Yongin 17104, Korea
These authors contributed equally: Chan Wook Jang, Won Jun Lee.

another approach, the top layer of Se in the pregrown $MoSe_2$ ML was sulfurized by a controlled substitution reaction with vaporized S[19]. The drawback of these methods is that they rely on follow-up treatments in addition to the initial chemical vapor deposition (CVD) of 2D MoS_2 or $MoSe_2$ TMDCs, which can result in increased complexity and cost. To overcome these limitations, we developed a new method of Janus MoSSe growth, simplified by employing a single NaCl-assisted process in a CVD apparatus. This approach involves three-step processes in situ to sequentially activate Mo and S for the growth of MoS_2, form S vacancies in the top MoS_2 layer, and activate Se to fill the vacancies only by altering the temperature (T) without using any other means, such as H_2 plasma[18]. Throughout the steps, the temperature in each chalcogen and transitional-metal zone was properly controlled, and NaCl lowered the melting point of the material. The grown Janus MoSSe was systemically examined by Raman scattering, photoluminescence (PL), atomic/Kelvin-probe force microscopy (AFM and KPFM), and optical microscopy (OM). Based on the experimental results, a possible growth mechanism is proposed. These results are believed to provide a simple, cost-effective, and universal approach for growing 2D Janus TMDCs; this approach is more useful for fundamental studies and device applications.

Materials and methods

Triangle-shaped 2D flakes were produced on 300 nm SiO_2/Si wafers by the NaCl-assisted vaporization of a mixture of MoO_3, S (or Se), and NaCl powders in a quartz tube furnace under a controlled gaseous environment. NaCl in the growth process was found to play a vital role in lowering the growth T[20,21]. A typical run of growth for MoS_2 was performed by loading 15 mg MoO_3 + 20 mg $NaCl_3$ powder in one boat in the high-T zone and 35 mg S powder in the other boat in the low-T zone within the same quartz tube. A piece of the SiO_2/Si substrate was placed at the downstream location close to the high-T boat. The low- and high-T zones in the furnace were heated to 150 and 750 °C, respectively, for 10 min; they were kept at these temperatures for 10 min for growing MoS_2. The vapor-phase reactants were transported by a mixed gas of H_2 and Ar, thereby facilitating the growth of the 2D crystals in the growth region. The flow rate of H_2 gas was fixed at 20 sccm. All the reactions were carried out at 10^{-1} Torr, and their heating rate was 25 °C min^{-1}. At the end of the growth phase, the furnace was left to naturally cool to room temperature. The procedure for synthesizing Janus MoSSe is detailed in the next section. To optimize the growth of Janus MoSSe, the distance between the boats and the rate of Ar gas were varied from 11 to 17 cm and 82 to 88 sccm, respectively.

Raman scattering and PL measurements were carried out using a confocal Raman/PL microscope (HEDA, NOST, Korea) with a 532 nm laser. A laser with a typical incident power of 100 μW was linearly polarized and focused to a spot size of < 1 μm by a 100× objective lens (numerical aperture, 0.9). The sample was mounted on a piezo-stepper table and scanned under the microscope. The spatial resolution of this setup was approximately 500 nm. The PL emission (or Raman scattering) signal was collected with the same objective, dispersed with a monochromator, and detected using a charge-coupled device (Andor Technology). The Raman scattering behaviors of MoSSe and $MoSe_2$ were also measured as a function of the polarization angle by employing a linear polarizer. The KPFM surface potential profiles and mapping images were obtained in the noncontact mode of an atomic force microscope (Park Systems model XE-100). The samples were transferred to indium tin oxide (ITO)-coated glasses for the KPFM measurements to prevent the problem of surface charging. The I-V curves were also obtained on ITO substrates in the conductive mode of the atomic force microscope.

Results and discussion

Figure 1a and b show the CVD apparatus for growing Janus MoSSe and a schematic diagram explaining the growth mechanism, respectively. The CVD system is divided into two zones, the low- and high-T zones, referred to as zones 1 and 2, respectively. The Se and S powders are located at separate positions in one boat, which is located in zone 1, while the other boat containing MoO_3 + NaCl powder and a SiO_2/Si substrate is located in zone 2. In the first step, a MoS_2 flake is synthesized on a SiO_2/Si substrate, where the Mo and S atoms are activated at $T = 750$ and 150 °C, respectively, in each zone (Supplementary Fig. S1). The grown MoS_2 flake showed typical Raman and PL spectra peaked at 382.6/406.4 cm^{-1} (E_{2g}/A_{1g} modes) and 691 nm, respectively (Fig. 2a and b), as previously reported[22–24]. The resulting difference between the Raman peaks was calculated to be 23.8 cm^{-1} and corresponded to a triple-layer MoS_2[25]. In the second step, S vacancies were formed in the MoS_2 flake (Fig. 1b), while the T in zone 2 was changed to 580 °C for 10 min without the addition of any activated atoms. This formation of vacancies was demonstrated in a separate annealing experiment, as described below. In the third step, the S vacancies in the top-surface MoS_2 were filled with Se atoms activated at $T = 300$ °C (Fig. 1b and Supplementary Fig. S1) to finally form Janus MoSSe. The vacancies were believed to be formed concomitantly in the layer during this last step, as was also demonstrated by the annealing experiment.

The growth of the Janus MoSSe layers was optimized through variation of the principal deposition parameters.
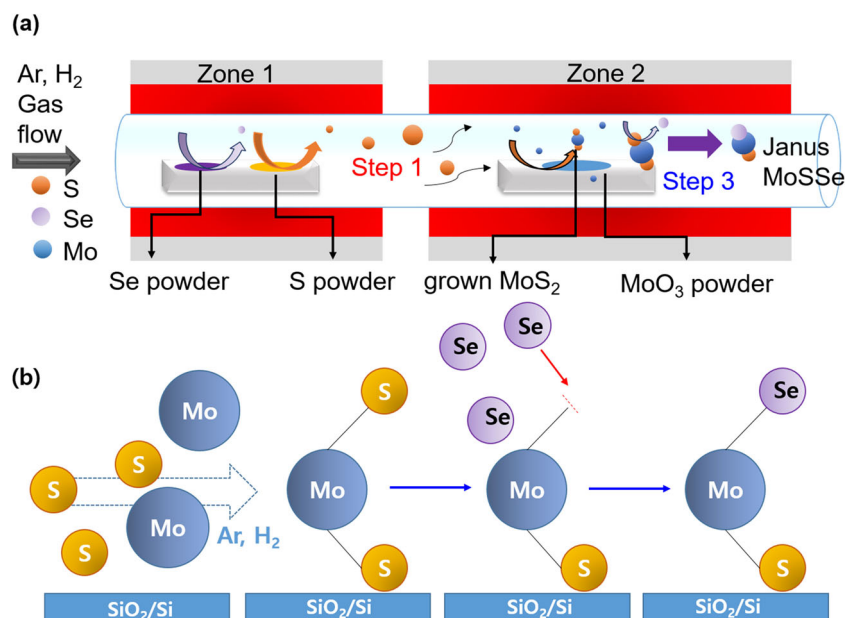
Fig. 1 Growth of Janus MoSSe. a CVD apparatus for Janus MoSSe. The CVD system is divided into two zones, zones 1 and 2. One boat for the Se and S powders is located in zone 1, while the other boat for the MoO_3 + NaCl powder and the SiO_2/Si substrate is located in zone 2. The Se and S powders are separated within the boat. **b** Schematic diagram detailing the growth mechanism. The in situ single growth process for MoSSe consists of three steps: synthesis of MoS_2 flakes, formation of S vacancies on the top-surface MoS_2 layer, and growth of Janus MoSSe.

During this procedure, the shape, size, and uniformity of the Janus MoSSe were shown to be very sensitive to a few major parameters, such as the distance (d) between the boats and the Ar flow rate (R_{Ar}). Figure 3 shows OM images of the flakes; these images were obtained by varying d at a fixed R_{Ar} of 86 sccm (see Supplementary Fig. S2 for the optimization through the variation of R_{Ar} at a fixed d of 15 cm) and the corresponding Raman and PL spectra. These results suggest that the Janus MoSSe with the best quality was fabricated under the optimized conditions: d = 15 cm and R_{Ar} = 86 sccm. As shown in the OM image of the optimized flake (Fig. 4a), the inner and outer regions are clearly distinguished by their triangular boundary between the layers. The Raman spectrum in the inner (or the outer) region exhibits major peaks at 287.2/350.2 (or 239.6/287.3) cm^{-1}, corresponding to the A_{1g}/E_{2g} modes of MoSSe (or $MoSe_2$), respectively[18,19,26], as shown in Fig. 3e (or Fig. 2a). The difference between the A_{1g} and E_{2g} modes of MoSSe is calculated to be approximately 63 cm^{-1}, which is very close to the theoretical and experimental values (~60 cm^{-1}) reported for a MoSSe monolayer[19,27,28]. Here, it should be noted that the MoS_2 peaks are also visible in the Raman spectrum of the inner region, indicating that the MoS_2 layer remains at the bottom of the Janus MoSSe even after optimization, resulting in the actual formation of a MoSSe/MoS_2 heterostructure.

Figures 2b and 3f show PL spectra of the inner and outer regions of the optimized flake. These spectra have peaks at 726 and 809 nm, which are consistent with those of MoSSe and $MoSe_2$, respectively[18,19,26]. As shown in the PL mapping images (Fig. 4b–c), the variation in the peak wavelength is clearly observed as the position moves in the direction from the inner region, the interface, to the outer region. This further demonstrates that the Janus MoSSe inside the flake is surrounded by the peripheral $MoSe_2$ region with the boundary between the regions. Near the boundary of the inner/outer regions, the intermediate PL and Raman spectra exhibited peaks corresponding to both MoSSe and $MoSe_2$ (Supplementary Fig. S3), resulting from the mixed phases of MoSSe and $MoSe_2$ near the boundary. As the position moves in the inner-to-outer region direction at the boundary, the Raman and PL peak intensities of MoSSe decrease, while those of $MoSe_2$ increase. Within the inner region, the PL peak redshifts in the center-to-edge direction (Fig. 4c).

Figure 4d–g and e–h compare the KPFM mapping images/surface potential profiles and AFM height profiles of MoS_2 and MoSSe. As shown in Fig. 4g, the potential profile of MoS_2 looks very uniform in the full region and is clearly differentiated from that of the substrate. Figure 4h shows a considerable change in the potential due to the formation of Janus MoSSe with respect to the substrate, together with a potential dip in the peripheral $MoSe_2$ region, consistent with the PL mapping images in Fig. 4b-c. The polarization-angle dependences of the Raman behaviors were measured for the polar plots of the peak intensities in the inner (MoSSe) and outer ($MoSe_2$) regions (Supplementary
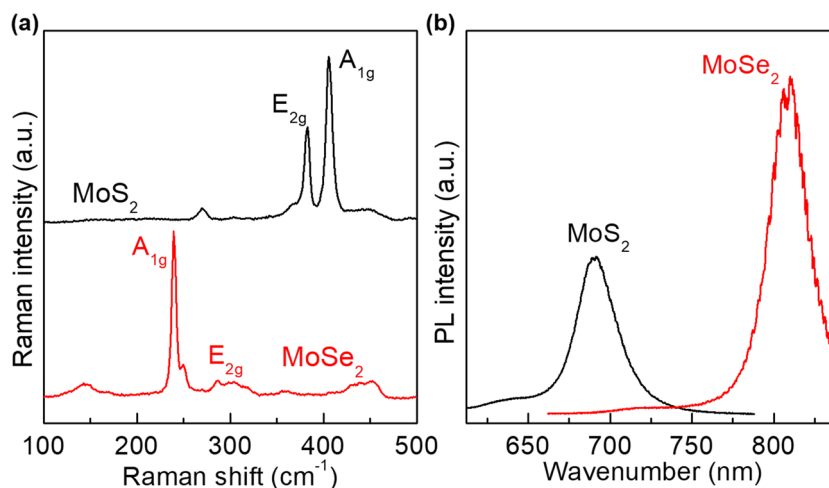
Fig. 2 Raman and PL spectra. a Raman and **b** PL spectra of the MoS_2 flake grown in the first step and the $MoSe_2$ in the peripheral region of the flake removed after the whole steps for the formation of the Janus MoSSe were finished. These spectra are consistent with those of MoS_2 and $MoSe_2$ reported in previous publications.
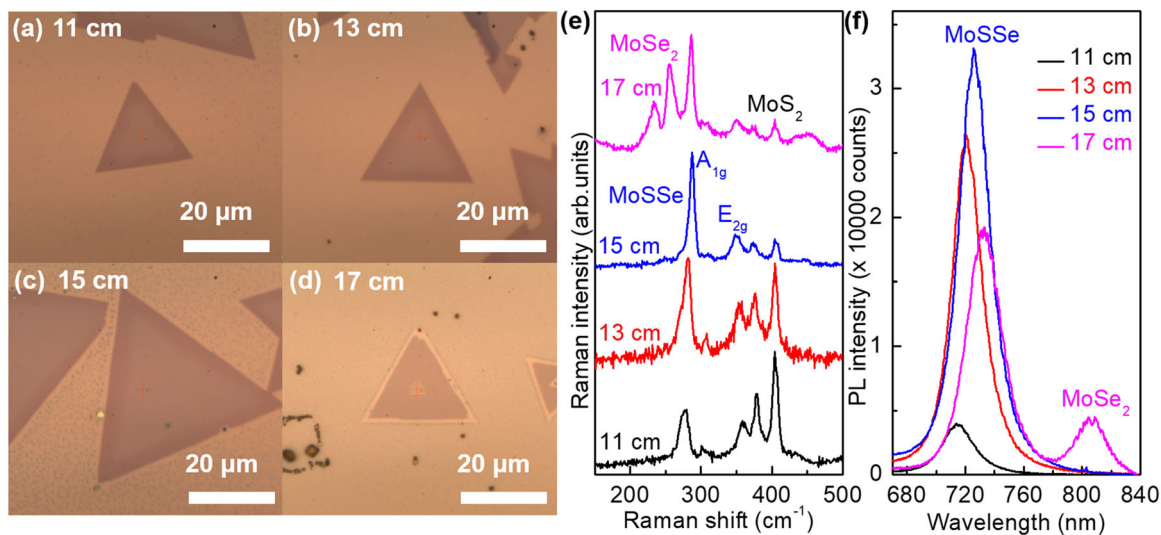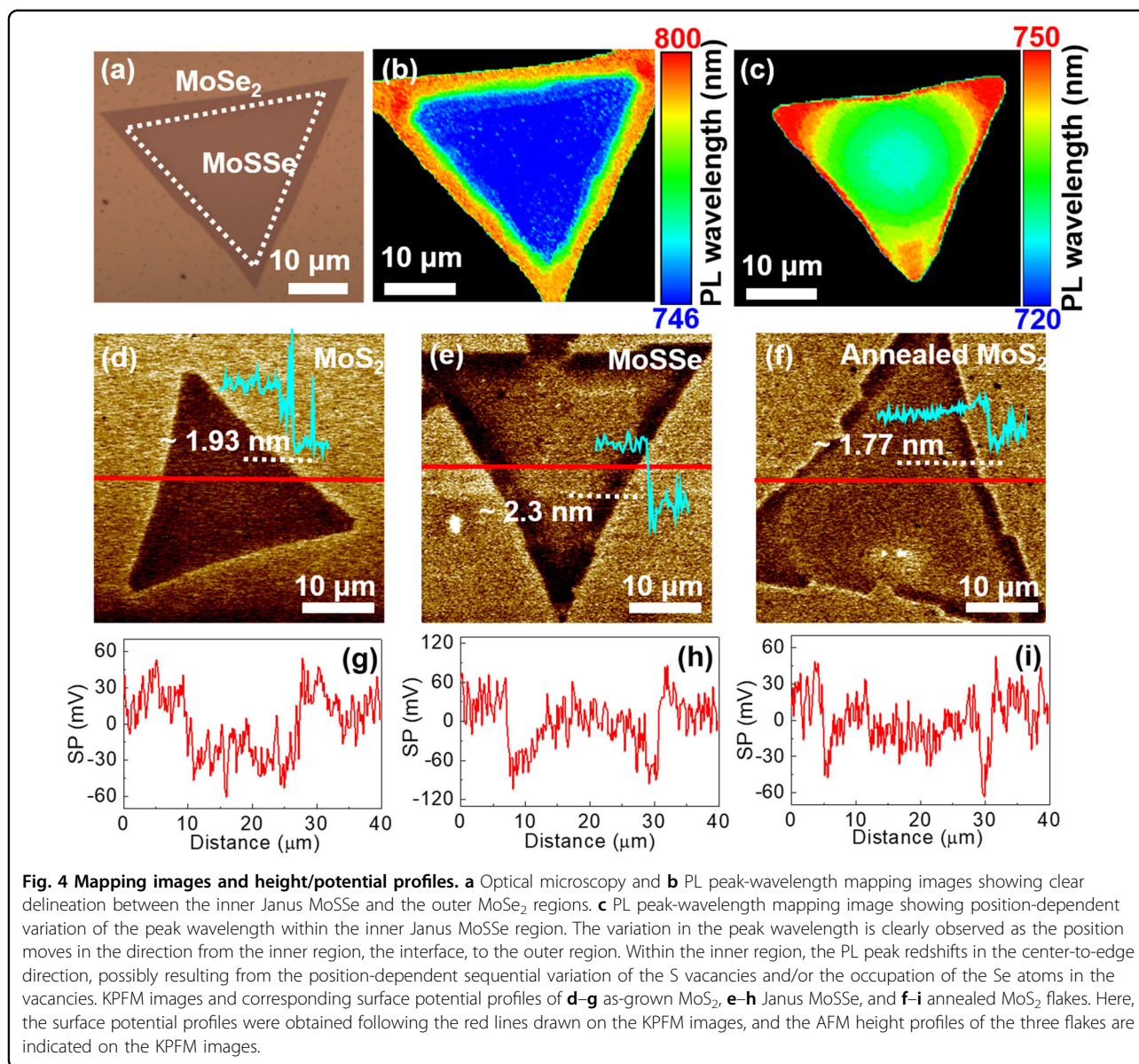

Fig. 3 Optimization of Janus MoSSe. a–d Optical microscopy images showing the Janus MoSSe flakes obtained by varying the distance between the boats in zones 1 and 2 from 11 to 17 cm, with the Ar flow rate fixed at 86 sccm for optimization, and **e–f** corresponding Raman and PL spectra (see Supplementary Fig. S2 for optimization by varying the Ar flow at a fixed d of 15 cm). These results suggest that the Janus MoSSe is optimized when the distance between the boats = 15 cm and the Ar rate = 86 sccm in this growing system.

Fig. S4). According to the Raman selection rules based on symmetry, the intensity of the E_{2g} mode was predicted to be independent of the polarization angle, while that of the A_{1g} mode was predicted to be polarized following the formula $I_{A1g} = A \cos^2\theta$, where I_{A1g} is the intensity, A is a constant, and θ is the angle[29]. This reasoning explains why the line shapes of the A_{1g} and E_{2g} modes were typical dumbbell and circular structures in the polar plots. Considerable differences in the polar plots between the MoSSe and $MoSe_2$ regions were not

observed, and this result was consistent with those of previous reports[29,30].

To analyze the conversion of MoS_2 to MoSSe, a separate annealing process was performed by keeping a grown MoS_2 flake at 580 °C (same T as was used for the growth of MoSSe) for 10 min in zone 2 without atomic activation under Ar flow. After annealing, almost no difference in the Raman spectrum of the MoS_2 flake was observed, but its PL spectrum was slightly redshifted (Supplementary Information, Fig. S5), which was consistent with a

Fig. 4 Mapping images and height/potential profiles. a Optical microscopy and **b** PL peak-wavelength mapping images showing clear delineation between the inner Janus MoSSe and the outer MoSe$_2$ regions. **c** PL peak-wavelength mapping image showing position-dependent variation of the peak wavelength within the inner Janus MoSSe region. The variation in the peak wavelength is clearly observed as the position moves in the direction from the inner region, the interface, to the outer region. Within the inner region, the PL peak redshifts in the center-to-edge direction, possibly resulting from the position-dependent sequential variation of the S vacancies and/or the occupation of the Se atoms in the vacancies. KPFM images and corresponding surface potential profiles of **d–g** as-grown MoS$_2$, **e–h** Janus MoSSe, and **f–i** annealed MoS$_2$ flakes. Here, the surface potential profiles were obtained following the red lines drawn on the KPFM images, and the AFM height profiles of the three flakes are indicated on the KPFM images.

previous report[31]. Figure 4d–g and f–i compare the KPFM mapping images and surface potential profiles of the grown and annealed MoS$_2$ flakes. A large change in the potential of MoS$_2$, including a sharp drop at the edge, was observed with respect to the substrate during annealing, as shown in Fig. 4i. In other words, the MoS$_2$ flake was fully changed by annealing, with the inner and peripheral parts being structurally different. No correlations between the KPFM results and the surface morphologies were observed, as confirmed by the AFM images (Supplementary Fig. S6). In addition, several vacant regions were identified in the annealed MoS$_2$ flake by OM and PL-mapping images (Supplementary Information, Fig. S7) and can be regarded as S vacancies, as previously reported[31–33]. These results demonstrate the formation of S

vacancies in the MoS$_2$ flake before and during the addition of activated Se (2nd & 3rd steps) in the fabrication process, as described above.

Mono- and bilayer MoS$_2$ flakes were also grown in the 1st step of Janus MoSSe fabrication, but after the 2nd and 3rd steps, no Janus MoSSe had formed, possibly due to the excessive thermal budget of these steps. This result further suggests that there is a critical minimum thickness for the successful growth of Janus MoSSe using our approach. Similar behaviors were reported in previous publications[33,34]. In these reports, the mono-layer MoS$_2$ was cracked when annealed above a critical temperature (this temperature depends on the approach). We also examined the samples after the 2nd step (similar to annealing); these samples included the mono- and bilayer

MoS_2 flakes grown in the 1st step. Almost no monolayer material remained, while for the bilayer, some MoS_2 debris was scattered on the SiO_2/Si surface (Supplementary Information, Fig. S8). To solve this problem, our system should be redesigned to reduce the excessive thermal budget, especially for the cases of the mono- or bilayer MoS_2. In contrast, the thermal load in thicker samples with ≥ 3 layers seems to be well distributed throughout the whole volume. The thick MoS_2 layer may also protect the Mo-S bond at the bottom. In addition, $MoSe_2$ formed in the peripheral region of the flake could act as a thermal barrier to reduce the thermal budget of the bottom Mo-S bond. This result explains why the breakage of the Mo-S bond at the surface was described when vacancies formed in the growth mechanism (Fig. 1b). If the annealing time and/or temperature is longer, even the bottom Mo-S bond will break. The optimum time and temperature for the Janus MoSSe were obtained after much trial and error.

The uniformity in the region of the Janus MoSSe was evaluated by measuring the PL and Raman spectra at different positions in the direction from the center to the vertex within the inner region of the triangular flake, as shown in Fig. 5a. Figure 5b, c show the position-dependent Raman spectra of MoSSe and MoS_2 in the inner region and the corresponding shifts of the A_{1g}/E_{2g} peak wavenumbers. Here, no considerable changes in the Raman peak energies were observed, as shown in Fig. 5c, but the main Raman peak ratio of $MoSSe/MoS_2$ decreased from the center to the vertex, as shown in Fig. 5b (and Supplementary Fig. S9a). The PL peak of MoSSe red-shifted in the same direction, as shown in Figs. 5d and 4c (and Supplementary Fig. S9b), and this result is very consistent with a previous report[33]. These results are possibly due to the position-dependent sequential variation of the S vacancies and/or the occupation of the Se atoms in the vacancies, as previously reported[31,32].

It is widely known that the crystalline structure is almost unchanged by the $MoS_2 \rightarrow MoSSe$ transformation, as shown in various publications[18,19]. The Janus MoSSe remains in a 2H crystalline phase even by the top layer S (or Se)-atom substitution of Se (or S) in $MoSe_2$ (or MoS_2), indicating that there is neither significant lattice distortion nor phase transition. Additionally, according to our results, the crystalline structure of the Janus MoSSe flake remained stable but its shape and size changed depending on the preparation conditions (Fig. 3 and Supplementary Fig. S2), as confirmed by the PL and Raman spectra. Even though other phases of Janus MoSSe, such as 1T or 1T′ exist, PL cannot be observed due to the metallic properties of the 1T or 1T′ phases, and their Raman spectra differ from that of the 2H phase, as shown in other 2D materials.
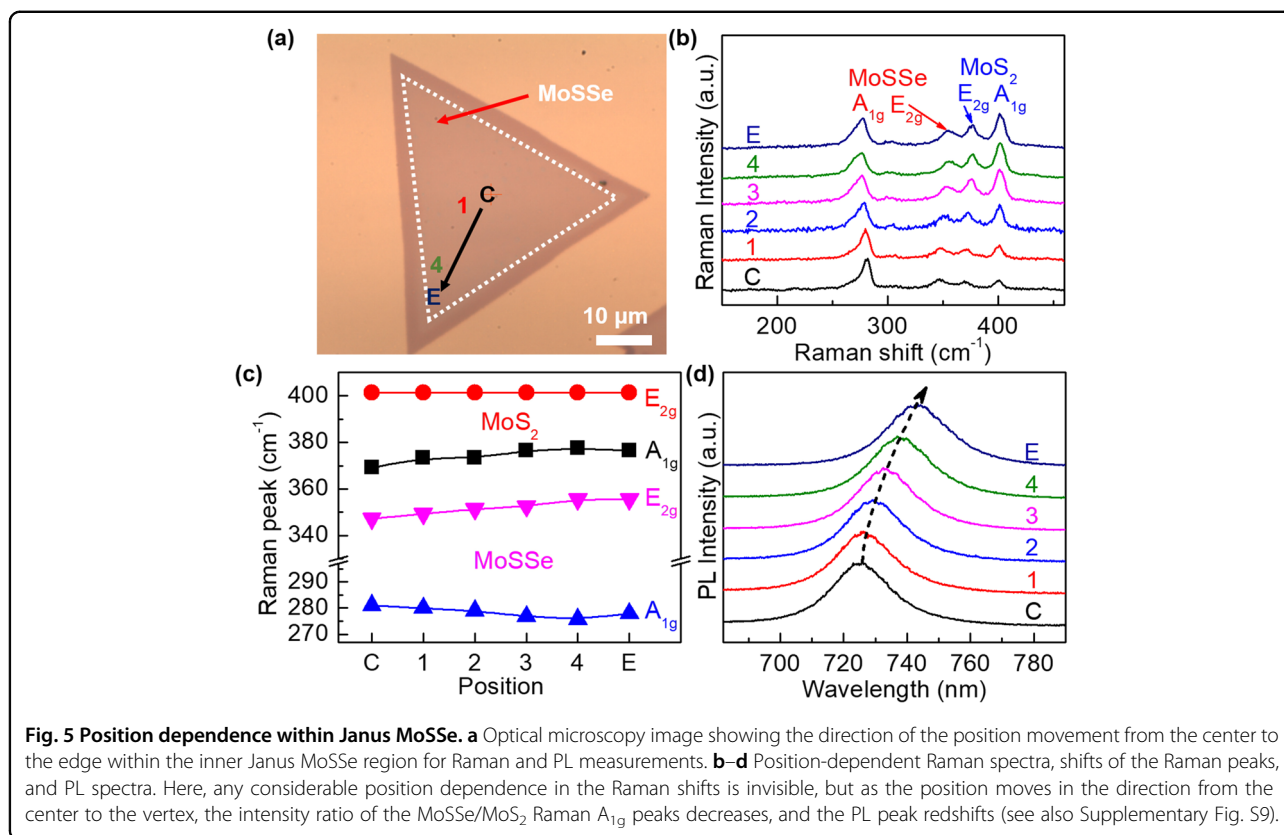
The shape of the 2D flakes is known to strongly depend on the preparation conditions[35−37], but most of the 2D flakes are predominantly triangle-shaped. For example, the crystal shape of the MoS_2 at equilibrium is hexagonal under Mo-rich conditions, while it becomes triangular under S-rich conditions[36]. More importantly, constructing larger and more uniform Janus crystals with the smallest possible defect density is a preeminent challenge. We accidentally succeeded in making Janus MoSSe with almost no peripheral $MoSe_2$ region (Supplementary Fig. S10), even though its preparation conditions needed to be further optimized for stabilization. In contrast, more S vacancies tended to form in hexagonal MoS_2 shapes, and their distributions gradually varied from the vertices and edges (triangular shape) to the center (hexagonal shape)[37]. Based on these findings, we focused on trying to make the Janus flakes as large and uniform as possible to secure a larger central MoSSe region in each triangular flake.

The I-V curves measured for the inner MoSSe and outer $MoSe_2$ regions showed rectifying behaviors, with steeper voltage-dependent current variation in the $MoSe_2$ region (Supplementary Fig. S11). Both layers formed heterojunctions with the bottom MoS_2 layer. The work function of MoS_2 was measured to be −4.85, −4.96, −5.09, and −5.13 eV for layer numbers 1, 2, 4, and 8, respectively, as was noted in our previous report[38]. Therefore, the work function of the bottom MoS_2 layer was estimated to be approximately −5.0 eV. The work function of monolayer $MoSe_2$ is known to be 4.70 eV[39]. The heterojunction of Janus MoSSe with MoS_2 is classified into two types: S/S and Se/S heterostructures[16]. The former corresponds to our case because the Se layer is at the top of the MoSSe. The work function of MoSSe in the S/S heterostructure was calculated to be −4.26 eV[16]. Based on these considerations, the barrier height of the $MoSe_2/MoS_2$ junction is lower than that of the $MoSSe/MoS_2$ junction, and this conclusion is consistent with the I-V behavior. These results are preliminary, so further in-depth characterization is needed to clarify the device properties of Janus MoSSe in future work.

Conclusion

We have shown the successful fabrication of Janus MoSSe by a new simplified method that employs a single NaCl-assisted process in a CVD apparatus. This approach involved three-step processes to sequentially activate Mo and S in situ to grow MoS_2, form S vacancies in the top-surface MoS_2 layer, and activate Se to fill the vacancies by only altering the temperature. The MoS_2 layer was shown to remain at the bottom of the Janus MoSSe even after optimization, resulting in the formation of a $MoSSe/MoS_2$ heterostructure. Throughout these steps, NaCl helped lower the melting points of the constituent substances, while the T in each zone was properly controlled. A possible growth mechanism was proposed based on the results of another annealing experiment that did not

Fig. 5 Position dependence within Janus MoSSe. a Optical microscopy image showing the direction of the position movement from the center to the edge within the inner Janus MoSSe region for Raman and PL measurements. **b–d** Position-dependent Raman spectra, shifts of the Raman peaks, and PL spectra. Here, any considerable position dependence in the Raman shifts is invisible, but as the position moves in the direction from the center to the vertex, the intensity ratio of the MoSSe/MoS$_2$ Raman A$_{1g}$ peaks decreases, and the PL peak redshifts (see also Supplementary Fig. S9).

supply activated atoms. This simple approach may open an easy way to fabricate various kinds of 2D Janus materials, which are very promising for their fundamental characteristics and applications in novel devices.

Author contributions
C.W.J. and W.J.L. prepared the 2D flakes and carried out the Raman and PL measurements. C.W.J. characterized the flakes by AFM and KPFM. J.K.K. performed the annealing experiments. S.M.P. obtained optical images of the flakes. S.K. analyzed the Raman and PL data. S.-H.C. initiated and supervised the work and wrote the paper. All authors discussed the results and commented on the manuscript.

Conflict of interest
The authors declare no competing interests.

References
1. Yagmurcukareds, M. et al. Quantum properties and applications of 2D Janus crystals and their superlattices. *Appl. Phys. Rev.* **7**, 011311 (2020).
2. Li, R., Cheng, Y. & Huang, W. Recent progress of Janus 2D transition metal chalcogenides: From theory to experiments. *Small* **14**, 1802091 (2018).
3. Zhang, L. et al. Recent advances in emerging Janus two dimensional materials: from fundamental physics to device applications. *J. Mater. Chem. A* **8**, 8813–8830 (2020).
4. Zheng, T. et al. Excitonic Dynamics in Janus MoSSe and WSSe Monolayers. *Nano Lett.* **21**, 931–937 (2021).
5. Wei, Y., Tang, X., Shang, J., Ju, L. & Kou, L. Two-dimensional functional materials: from properties to potential applications. *Int. J. Smart Nano Mater.* **11**, 247–264 (2020).
6. Wang, J. et al. Intriguing electronic and optical properties of two-dimensional Janus transition metal dichalcogenides. *Phys. Chem. Chem. Phys.* **20**, 18571–18578 (2018).
7. Han, L. et al. Anomalous behavior of 2D Janus excitonic layers under extreme pressures. *Adv. Mater.* **32**, 2002401 (2020).
8. Ko, K. Y. et al. High-performance gas sensor using a large-area WS$_{2x}$Se$_{2−2x}$ alloy for low-power operation wearable applications. *ACS Appl. Mater. Interfaces* **10**, 34163–34171 (2018).
9. Liu, Y.-L., Shi, Y. & Yang, C.-L. Two-dimensional MoSSe/g-GeC van der waals heterostructure as promising multifunctional system for solar energy conversion. *Appl. Surf. Sci.* **545**, 148952 (2021).
10. Ju, L., Bie, M., Shang, J., Tang, X. & Kou, L. Janus transition metal dichalcogenides: a superior platform for photocatalytic water splitting. *J. Phys. Mater.* **3**, 022004 (2020).
11. Dong, L., Lou, J. & Shenoy, V. B. Large in-plane and vertical piezoelectricity in Janus transition metal dichalchogenides. *ACS Nano* **11**, 8242–8248 (2017).
12. Li, L. et al. Wavelength-tunable interlayer exciton emission at the near-infrared region in van der Waals semiconductor heterostructures. *Nano Lett.* **20**, 3361–3368 (2020).

13. Le, C. T. et al. Effects of interlayer coupling and band offset on second harmonic generation in vertical $MoS_2/MoS_{2(1-x)}Se_{2x}$ structures. *ACS Nano* **14**, 4366–4373 (2020).

14. Riis-Jensen, A. C., Pandey, M. & Thygesen, K. S. Efficient charge separation in 2D Janus van der Waals structures with built-in electric fields and intrinsic p−n doping. *J. Phys. Chem. C.* **122**, 24520–24526 (2018).

15. Palsgaard, M., Gunst, T., Markussen, T., Thygesen, K. S. & Brandbyge, M. Stacked Janus device concepts: Abrupt pn-junctions and cross-plane channels. *Nano Lett.* **18**, 7275–7281 (2018).

16. Zhang, K. et al. Efthimios Kaxiras, Spectroscopic signatures of interlayer coupling in Janus $MoSSe/MoS_2$ heterostructures. *ACS Nano* **15**, 14394–14403 (2021).

17. Cavalcante, L. S. R., Gjerding, M. N., Chaves, A. & Thygesen, K. S. Enhancing and controlling plasmons in Janus MoSSe—Graphene based van der Waals heterostructures. *J. Phys. Chem. C.* **123**, 16373–16379 (2019).

18. Lu, A.-Y. et al. Janus monolayers of transition metal dichalcogenides. *Nat. Nanotechnol.* **12**, 744–749 (2017).

19. Zhang, J. et al. Janus monolayer transition-metal dichalcogenides. *ACS Nano* **11**, 8192–8198 (2017).

20. Zhou, J. et al. A library of atomically thin metal chalcogenides. *Nature* **556**, 355–359 (2018).

21. Wang, Z. et al. NaCl-assisted one-step growth of MoS_2–WS_2 in-plane heterostructures. *Nanotechnology* **28**, 325602 (2017).

22. Chen, H. et al. Ultrafast formation of interlayer hot excitons in atomically thin MoS_2/WS_2 heterostructures. *Nat. Commun.* **7**, 12512 (2016).

23. Zhang, J. et al. Interlayer-state-coupling dependent ultrafast charge transfer in MoS_2/WS_2 bilayers. *Adv. Sci.* **4**, 1700086 (2017).

24. Pawbake, A. S., Pawar, M. S., Jadkar, S. R. & Late, D. J. Large area chemical vapor deposition of monolayer transition metal dichalcogenides and their temperature dependent Raman spectroscopy studies. *Nanoscale* **8**, 3008–3018 (2016).

25. Kandemir, A., Peeters, F. M. & Sahin, H. Monitoring the effect of asymmetrical vertical strain on Janus single layers of MoSSe via vibrational spectrum. *J. Chem. Phys.* **149**, 084707 (2018).

26. Taghizadeh, A., Leffers, U., Pedersen, T. G. & Thygesen, K. S. A library of ab initio Raman spectra for automated identification of 2D materials. *Nat. Commun.* **11**, 3011 (2020).

27. Lee, C. et al. Anomalous lattice vibrations of single-and few-layer MoS_2. *ACS Nano* **4**, 2695–2700 (2010).

28. Zhao, Y., Lee, H., Choi, W., Fei, W. & Lee, C. J. Large-area synthesis of monolayer $MoSe_2$ films on SiO_2/Si substrates by atmospheric pressure chemical vapor deposition. *RSC Adv.* **7**, 27969–27973 (2017).

29. Petrić, M. M. et al. Raman spectrum of Janus transition metal dichalcogenide monolayers WSSe and MoSSe. *Phys. Rev. B* **103**, 035414 (2021).

30. Zhao, S. et al. A Se vacancy induced localized Raman mode in two-dimensional $MoSe_2$ grown by CVD. arXiv.1904.09789 (2019).

31. Yanase, T., Uehara, F., Naito, I., Nagahama, T. & Shimada, T. Healing sulfur vacancies in monolayer MoS_2 by high-pressure sulfur and selenium annealing: Implication for high-performance transistor. *ACS Appl. Nano Mater.* **3**, 10462–10469 (2020).

32. Wang, L., Ji, X., Chen, F. & Zhang, Q. Temperature-dependent properties of monolayer MoS_2 annealed in an Ar diluted S atmosphere: an experimental and first-principles study. *J. Mater. Chem. C.* **5**, 11138–11143 (2017).

33. Li, H. et al. Lateral growth of composition graded atomic layer $MoS_{2(1-x)}Se_{2x}$ nanosheets. *J. Am. Chem. Soc.* **137**, 5284–5287 (2015).

34. Pitthan, E., Gerling, E. R. F., Feijó, T. O., Radtke, C. & Soares, G. V. Annealing response of monolayer MoS_2 grown by chemical vapor deposition. *ECS J. Solid State Sci. Technol.* **8**, P267–P270 (2019).

35. Zhu, S. & Wang, Q. A simple method for understanding the triangular growth patterns of transition metal dichalcogenide sheets. *AIP Adv.* **5**, 107105 (2015).

36. Raju, M., Wan, M., Sen, S. & Jacob, C. Influence of chemical potential on shape evolution of 2D-MoS_2 flakes produced by chemical vapor deposition. *Nanotechnology* **32**, 045301 (2021).

37. Zhang, G. et al. Shape-dependent defect structures of monolayer MoS_2 crystals grown by chemical vapor deposition. *ACS Appl. Mater. Interfaces* **9**, 1763–1770 (2017).

38. Shin, D. H., Jang, C. W., Ko, J. S. & Choi, S.-H. Enhancement of efficiency and stability in organic solar cells by employing MoS_2 transport layer, graphene electrode, and graphene quantum dots-added active layer. *Appl. Surf. Sci.* **538**, 148155 (2021).

39. Pan, Y. J. et al. Interfacial properties of monolayer $MoSe_2$-metal contacts. *J. Phys. Chem. C.* **120**, 13063–13070 (2016).